Ballooning versus curling of mantle plumes: views from numerical models

Urmi Dutta, Shamik Sarkar and Nibir Mandal*

Department of Geological Sciences, Jadavpur University, Kolkata 700 032, India

Mantle plumes constitute a large-scale thermal advection process of million-year timescale inside the Earth. It has been inferred that they mostly initiate as thermal perturbations at the core–mantle boundary, and subsequently ascend through the mantle, giving rise to hotspots and large igneous provinces. Using volume-of-fluid (VOF) models, the present study provides a new insight into the issue – ballooning versus curling mode of plume ascent. Earlier models have predicted curling to ballooning transitions with increasing mantle–plume viscosity contrast. Our thermo-mechanical model simulations demonstrate this transition as a function of two independent physical variables: density contrast ($\Delta\rho = \rho_a/\rho_p$, ρ_a and ρ_p are mantle and plume density respectively) and material influx rate (normalized in terms of Reynolds number *Re*). The ballooning mode occurs in a condition of high $\Delta\rho$ (~ 1.2) and low *Re* (~ 6), which transforms into the curling mode as the condition is reversed ($\Delta\rho$ = 1.1 and *Re* = 18). In this study we mapped the temperature distribution in and around plumes, and compared their thermal structures with those defined by the phase boundary. The thermal maps do not manifest their strong curling behaviour, suggesting that seismic tomography perhaps reveals the thermal boundary of natural plumes, rather than the mantle–plume phase boundary.

Keywords: Convection, density contrast, phase and thermal boundary, plume head, thermal buoyancy.

Introduction

IN the Earth's interior thermo-mechanical instabilities take place at the core–mantle boundary (a seismically distinct zone, called *D″*), resulting in upwelling of hot and buoyant mantle materials in the form of thermal plumes[1]. Many geoscientists have hypothesized the origin of large igneous provinces such as the Deccan Traps and the Siberian Traps[2], and hotspots such as Iceland and Hawaiian Islands[3] around the globe as a surface manifestation of thermally driven plumes. Consequently, understanding the mechanics of mantle plumes has triggered renewed research interest in the last couple of decades. According to the classical theory, thermal anomalies cause the density to drop locally, forming buoyant zones, which ascend through the heavier mantle ambience. Turcotte and Schubert[4] have theorized the ascent velocity of thermal plumes, considering an ideal spherical shape of its head trailing to a cylindrical tail. According to their theoretical model, the plume head maintains a constant size, and ascends with a constant velocity under a steady-state mass supply into the tail. However, the ascent processes appear to be unsteady and much more complex, as evident from a large volume of later numerical and physical model experiments[5–7]. Such complex ascent behaviour results mainly from a thermally as well as chemically stratified structure of the Earth's mantle. Some workers have shown the initiation of secondary plumes in the chemical boundary layer between the lower and upper mantle[8–10]. It has been proposed that these secondary plumes originate from the thermo-chemical instabilities in the halted plumes at the 670 km discontinuity. Furthermore, this mantle discontinuity can act as a potential mechanical zone where ascending plumes in the lower mantle undergo discernible shape changes of their head or sharp deflections of the tails[11–16].

An important line of plume research has been driven largely by laboratory experiments on analogue models, which primarily aim to study the geometrical evolution of buoyant plumes. The experiments reveal two principal geometrical varieties of plumes with their heads much larger than the corresponding tails in diameter: (1) balloon-shaped and (2) mushroom-shaped (Figure 1). These two principal varieties have been widely reported from numerical[7,17–20] and physical models[5,21,22]. We review briefly recent models to discuss important factors controlling the development of mantle plumes of varying shapes. The viscosity ratio (R) between plume and ambient mantle materials has been shown as a crucial physical parameter in many studies. From experimental studies, Olson and Singer[23] have demonstrated the evolution of mushroom-shaped plumes for low R, which transform into balloon-shaped plumes as R becomes large. A similar line of experimental observations was reported by later workers like Whitehead and Luther[24]. However, all these studies did not specifically account for the temperature effect on plume viscosity. Kellogg and King[25] have dealt with the temperature-dependent viscosity to show the development of contrasting plume shapes. According to their models, plumes with constant or weakly temperature-

*For correspondence. (e-mail: nibirmandal@yahoo.co.in)

dependent viscosity are unlikely to evolve with a typical head–tail configuration. On the other hand, strongly temperature-dependent viscosity conditions produce plumes with mushroom-shaped heads. Using the numerical model, Kumagai[26] studied the nature of interaction between ascending plume heads and the ambient mantle materials by increasing the mantle–plume viscosity ratio R. For low R (~ 10) plumes form vortex rings, giving rise to heads with multilayered, volute structures. With increasing R the heads involve mingling of mantle materials, described as stirring type of plumes. The mingling becomes restricted to a narrow zone at the lower part of plume heads when $R > 700$. It appears from their experimental results that increasing viscosity contrast promotes the ballooning type in preference to the curling type. Later workers have advanced plume models by including several additional physical parameters, and demonstrated the development of much more complex plume geometry (see Ribe *et al.*[27]).

Most of the models discussed above explain the mechanics of mantle plumes in terms of thermal buoyancy forces. However, ascending plume materials can undergo mineralogical transformations, e.g. perovskite to ringwoodite with decreasing pressure and temperature. Such transformations can result in the lowering of plume density, which consequently leads to an additional buoyancy in the ascending plume and thereby controls the plume

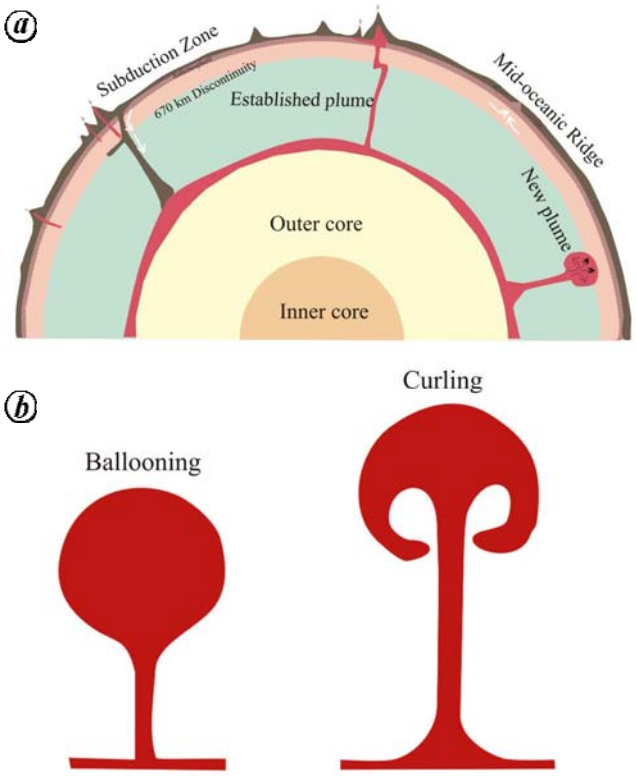

Figure 1. ***a***, A cartoon diagram of thermal plumes rooted to D'' layer at the core–mantle boundary. ***b***, Two principal modes of plume ascent by ballooning and curling of the heads.

shapes[7]. Lin and van Keken[7] have classified mantle plumes into three categories, and explained their transitions as functions of the compositional basal layer (CBL) and the high density layer (HDL) thicknesses. For a constant thermal boundary layer (TBL) thickness, plumes grow with mushroom-shaped head trailing to a narrow cylindrical tail when the HDL thickness is less than or equal to 80 km, but develop a discernible topographical relief at the TBL, giving rise to tail with inverted funnel structure when the CBL thickness ≥ 100 km. Plumes develop secondary instabilities, forming minor heads below the principal head when the CBL is very thick. Furthermore, the ratio of chemical and thermal buoyancy forces can greatly control the evolution of plume shapes[28]. An increase in this buoyancy ratio (0–1.25) shows a transition of mushroom-shaped regular geometry to patchy and irregular geometry. This study possibly explains the origin of patchy occurrences of mantle plumes beneath several hotspots, such as Hawaiian.

Most of the numerical models treat the mantle as incompressible and iso-viscous or temperature-dependent viscous[7,29–32]. However, seismic studies suggest that the mantle in reality is compressible[33–35]. Increasing pressure with depth can greatly influence the physical parameters, namely density, viscosity and thermodynamic properties of plume materials controlling the evolution of plume shapes, as suggested from petrological and geophysical investigations, e.g. long wavelength geoid anomalies across subduction zones and hotspots[36–38]. In a recent study, Leng and Gurnis[35] have predicted a reduction in the size of plume head due to decreasing viscosity from the core–mantle boundary to the base of the lithosphere. Their estimates show that the plume head can undergo size reduction even by 40% when a low-viscosity zone occurs between 100 and 660 km depth.

The theoretical and numerical models discussed above account fundamentally for the buoyancy, resulting from either thermal or chemical changes as the main driving forces. However, injection models[39] in fluid mechanics show that low-viscosity bubbles (cf. plumes) of contrasting shapes (e.g. typical head–tail versus discrete bulbous structure) can develop depending upon the injection velocity, i.e. the rate of material inflow. This type of fluid model suggests that the viscous forces, exerted by the upward flow of plume material through the tail can be an additional factor in controlling the ascent process of plumes in the mantle. It may be recalled that the material influx into a plume can depend on a number of geological factors, such as chemical boundary layer thickness and the presence of HDL within the TBL[7]. Using volume of fluid (VOF) models we show the conditions for ballooning versus curling mode of plume ascent taking into account the effects of influx rates, in addition to density and viscosity contrasts. Despite a huge volume of literature on plumes, it is yet to address why mushroom-shaped plumes are rarely detected from geophysical observations

although these are the most common type obtained in numerical simulations. Here we discuss this burning issue, suggesting that seismic tomographs probably provide plume shapes defined by thermal boundaries, rather than any phase boundaries.

Theoretical approach

Concept of VOF method

The fluid VOF method, first introduced by Hirt and Nichols[40], has been widely used in modelling the flow behaviour of multiphase systems. The fundamental principle of this method involves volume averaging of multiphase fluids in describing the flow equations. This theoretical treatment tracks the interfaces of two fluid phases with the help of a phase indicator function γ (also denoted as colour function or volume fraction). $\gamma = 1$ implies a phase, say phase 1, whereas $\gamma = 0$ indicates another phase, say phase 2. The interface domain between two phases can be tracked with the value of γ lying between 0 and 1 (Figure 2 *a*). The method has been implemented using the computational fluid dynamics (CFD) code FLUENT[41–43]. The VOF formulation assumes that the fluid phases taken for modelling remain in the immiscible state.

Governing equations

The VOF method uses a set of basic equations in fluid mechanics. A brief description of the three principal equations is given below. The theoretical formulation imposes the condition of mass balance in space and time, considering a volume average of fluid volumes. The expression of mass balance equation follows

$$\frac{\partial \rho}{\partial t} + \nabla \cdot (\rho v) = 0, \tag{1}$$

where the density parameter ρ is defined by the phase indicator function γ as

$$\rho = \{\gamma\rho_1 + (1 - \gamma)\rho_2\}. \tag{2}$$

For $\gamma = 0$, $\rho = \rho_2$ (phase 2) and $\gamma = 1$, $\rho = \rho_1$ (phase 1). For the interface domain, $0 < \gamma < 1$. With the same volume approach the formulation exercises the momentum equation, the expression of which is

$$\frac{\partial}{\partial t}(\rho\vec{v}) + \nabla \cdot (\rho\vec{v}\vec{v}) = \nabla \cdot (T) + \rho g + F. \tag{3}$$

T is the deviatoric stress, $\vec{v}$ denotes the velocity vector and F stands for the body force term. Equation (3) is the most important equation to describe the dynamics of multiphase flow. The VOF method introduces an energy balance of the multiphase system in space and time, which is also expressed by volume averaging as

$$\frac{\partial}{\partial t}(\rho E) + \nabla(\vec{v}(\rho E + p)) = \nabla(k_{\text{eff}} \nabla T) + S_h, \tag{4}$$

where E, T and k_{eff} are the energy, temperature and effective conductivity respectively. E can be also treated as mass-averaged variables

$$E = \frac{\sum_{q=1}^{n} \gamma_q \rho_q E_q}{\sum_{q=1}^{n} \gamma_q \rho_q}. \tag{5}$$

Non-dimensionalization of physical parameters

This kind of fluid mechanical problem demands non-dimensionalization of the different parameters to universalize the theoretical as well as computational treatments. In our studies we have modelled the multiphase system consisting of a low-viscosity (coefficient of kinematic viscosity, μ_p) fluid phase (phase 2) within a high-viscosity (coefficient of kinematic viscosity, μ_a) fluid phase (phase 1). The density of phase 2 (ρ_p) is lower than that of phase 1 (ρ_a). Plumes were simulated in the VOF models by injecting phase 2 into the phase 1 space with a specified velocity V_i. We varied V_i in our model experiments to investigate the control of volume influx into the tail in the development of plume shapes. The effect of injecting velocity on plume development can be dealt with an equivalent non-dimensional parameter, namely Reynolds number (*Re*), the expression of which follows

$$Re = \frac{\rho_p V_i d}{\mu_p}. \tag{6}$$

In our model we varied *Re* from 5 to 20 by varying V_i, keeping all other parameters constant so as to show exclusively the effects of volume influx rate in terms of the non-dimensional quantity *Re*. We considered a power-law function in describing the temperature dependent viscosity[44–46]. According to this law, the relation between the coefficient of viscosity and temperature is expressed in terms of an exponent factor as

$$\mu = \mu_0 \left(\frac{T}{T_0}\right)^{-n}, \tag{7}$$

where n is an empirical exponent factor. For the mantle conditions[7] the range of n is in the order of 0–3. μ_0 is the viscosity corresponding to the reference temperature T_0. It has been discussed in the preceding section that the viscosity contrast between the plume and mantle materials has large controls on the evolution of plume shapes.

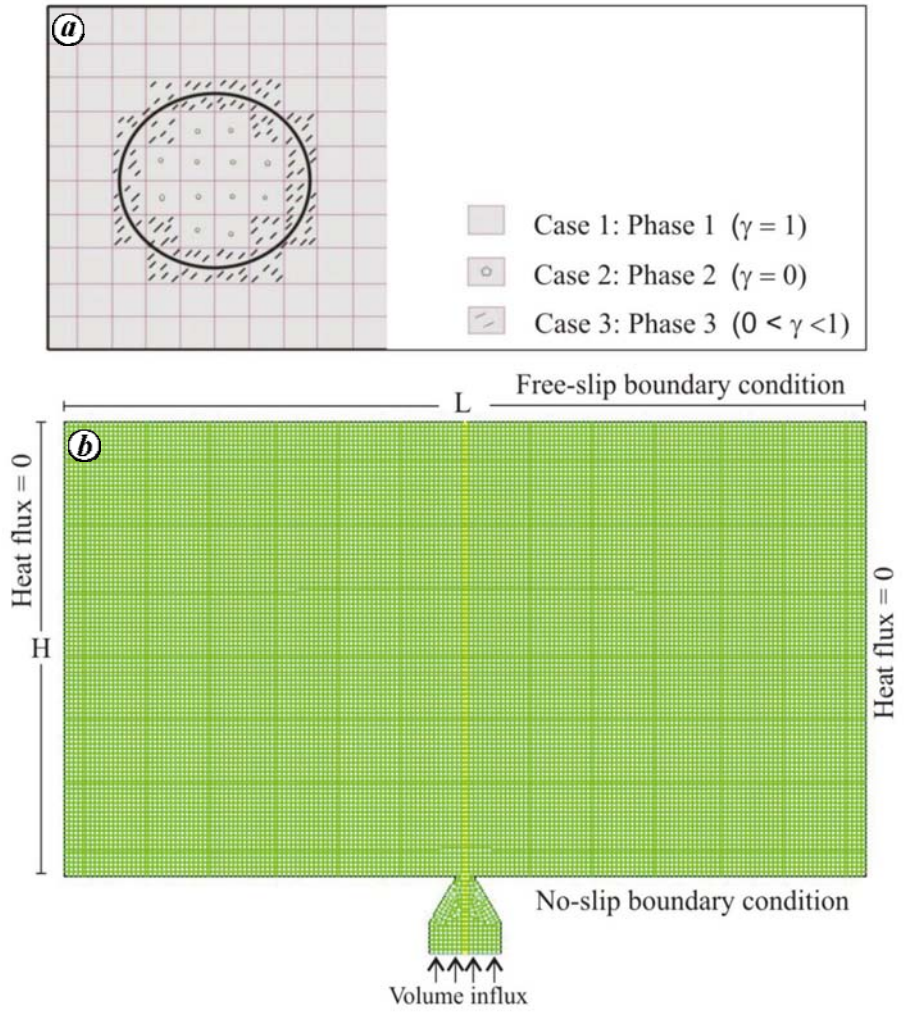

Figure 2. ***a***, Basic mathematical concept of volume averaging in a two-phase fluid system. γ is a phase indicator function (see text for details). ***b***, An initial volume-of-fluid (VOF) model showing the boundary conditions chosen for numerical simulation.

In our models we consider this factor as a non-dimensional quantity by taking the ratio of mantle and plume viscosities

$$R = \frac{\mu_a}{\mu_p}. \tag{8}$$

R was varied between 1 and 5. The Boussinesq model was adopted to account for the effects of temperature on density. According to this model, the fluid density holds the following relation

$$(\rho_p - \rho_a)g \approx -\rho_a \beta (T_p - T_a)g, \tag{9}$$

where β is the thermal expansion coefficient, and T_p and T_a are plume temperature and the surface temperature in ambient medium respectively. The density contrast ($\Delta\rho$) has been considered as a non-dimensional quantity as

$$\Delta\rho = \frac{\rho_a}{\rho_p}. \tag{10}$$

In our calculations, temperature has been normalized in following way

$$T^* = \frac{T}{(T_p)_{\text{initial}}}, \tag{11}$$

T stands for the calculated temperature at any given point and $(T_p)_{\text{initial}}$ is the initial temperature of the plume material injected into the mantle medium. In thermo-mechanical problems, Prandtl number (Pr) has been widely used to show the viscous movements relative to thermal diffusion rates. It is expressed as the ratio of viscous and thermal diffusion rates

$$Pr = \frac{c_p \mu}{k}. \tag{12}$$

Small Pr values imply that heat diffuses at mush faster rates, compared to the mechanical velocity (momentum). C_p and k are the specific heat and the thermal conducti-

vity respectively. In contrast, high *Pr* values indicate strong convective motion in the system. *Pr* for the Earth's mantle is estimated in the order of 10^{25}, suggesting convection dominating over the thermal diffusion processes. In this study we evaluated *Pr* associated with thermal plumes in the mantle, and obtained its values in the order of 10^{22} (ref. 47).

Model set-up

We chose a two-dimensional Eulerian reference scheme in describing the fluid phases for VOF model simulations. The models had a global phase (phase 1) space covering a depth equivalent to the mantle thickness (~ 2900 km) and a width of 1.5 times the mantle thickness. The model had a small region at the centre of its base containing plume material (phase 2), connected through an orifice with the diameter equivalent to a plume tail diameter of about 100 km. We considered an axisymmetric plume structure in our modelling. A free-slip condition was imposed upon the top, whereas a non-slip condition at the basal surface (Figure 2 *b*). The top and bottom surfaces were subjected to contrasting temperatures, T_t and T_b, where $T_b \gg T_t$. We impose a condition of no heat or mass flux across the lateral model boundaries. The two fluids were treated as mechanically distinct phases, undergoing a mutual interaction through surface tension. We varied the viscosity ratio of two fluid phases in different simulations. In the experiments, we always chose $R \geq 1$, as the ambient mantle viscosity is generally greater than that of the plume material. Details of different model parameters are given in Table 1.

The model was finely meshed with grid size equivalent to a real space of 25 km × 25 km employing a Lagrangian reference frame. The mesh was of tetrahedron (patch conforming) type. Each grid was sufficiently smaller than the plume size, giving a good approximation for heterogeneous mechanical and thermal states in the model.

Model results and discussion

We performed simulations by varying the density contrast factor ($\Delta\rho$) and the material influx rate into the plume tail

Table 1. Physical properties of the materials used in the numerical simulations

Symbol	Physical properties	Values
$\Delta\rho = \rho_a/\rho_p$	Density contrast	1.1–1.2
$R = \mu_a/\mu_p$	Viscosity ratio	1–5
C_p	Specific heat	1600 J/kg-K
K	Thermal conductivity	2 W/m-K
$Pr = c_p\mu/k$	Prandtl number	$2.4–4 \times 10^{22}$
β	Thermal expansion coefficient	5×10^{-5}/K
H	Model depth	~ 2900 km
L	Model width	~ 4350 km
$T^* = T/(T_p)_{\text{initial}}$	Normalized model temperature	0.4–1.0

(*Re*). In order to show exclusively the effects of these two parameters on the plume shapes, the model results obtained for little or no viscosity contrast ($R \sim 1$) are also presented here for a direct comparison. The prime aim of our simulations is to show the conditions for two principal modes of plume ascent: ballooning and curling as a function of density contrast and material influx rate. In this study we deal with the plume shapes by mapping the phase boundary, i.e. physical boundary between plume and mantle materials and the thermal boundary, i.e. temperature-defined boundary. Evidently, the physical and thermal plume structures significantly differ from each other.

Effects of density contrast and influx rate

Model simulations with relatively large density contrast ($\Delta\rho > 1.2$) and low influx rates ($Re \sim 6$) produced a ballooning-type plume shape, obtained from the phase boundary mapping (Figure 3 *a*). The model plume formed initially with a distinct head-and-tail structure. However, the ballooning process progressively dominated over the vertical growth of the tail, and developed a large head trailing into an incipient tail, resembling bulbous structures (Figure 3 *a*), as reported by several previous workers (e.g. Lin and van Keken[7]). Entrainment of the ambient material into the growing plume head is a geodynamic process of much interest, as it has large implications in characterizing material mixing phenomena and their effects on geochemical signatures of plume-related hotspots. Our model shows that the material entrainment in the ballooning mode is virtually absent, as noticed from the phase boundary dispositions at successive stages of the model plume. The thermal structure grossly tracks the phase boundary, especially at the early stage of evolution (Figure 3 *b*). However, a close inspection reveals thermal heterogeneity, showing localization of the highest temperature in the form of mushroom-shaped geometry connected to a cylindrical tail. However, it may not be possible to detect such geometry from any geophysical technique such as seismic tomography, as the temperature contrast is low ($\Delta T^* < 0.3$). The thermal boundary shows a conspicuous departure from the phase boundary at the meeting point between the head and tail, forming wavelike perturbations growing laterally with time. We evaluated the patterns of density and viscosity variations across the plume, which conform to those defined by the thermal boundary. These patterns are thus not shown separately.

For the same density contrast ($\Delta\rho = 1.2$), the mode of plume ascent underwent significant changes when the influx rate (*Re*) was increased. For $Re = 18$, the ballooning mode weakened, whereas the vertical growth of the tail strengthened, resulting in a plume with a small head trailing into a long, slender tail (Figure 4 *a*). The head started to grow only when it approached the model surface. The

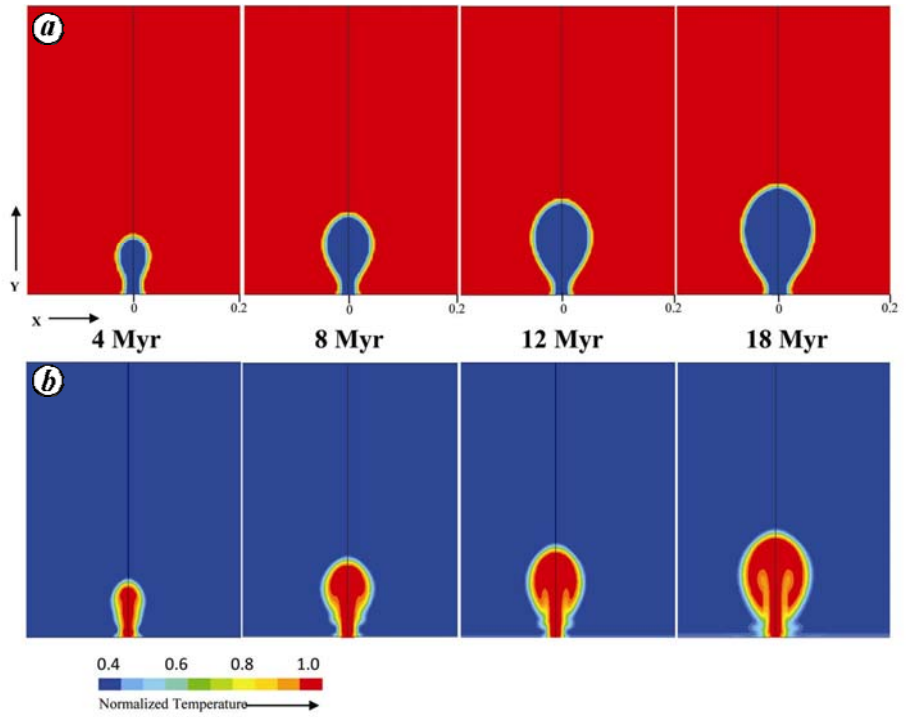

Figure 3. Progressive development of a plume in ballooning mode in VOF models run with high density contrast ($\Delta\rho$ = 1.2) and low influx rate (Re = 6). Viscosity ratio R = 1. Mapping of the plume shapes by (***a***) phase and (***b***) thermal boundary. The temperature scale has been normalized by the initial temperature of plume material.

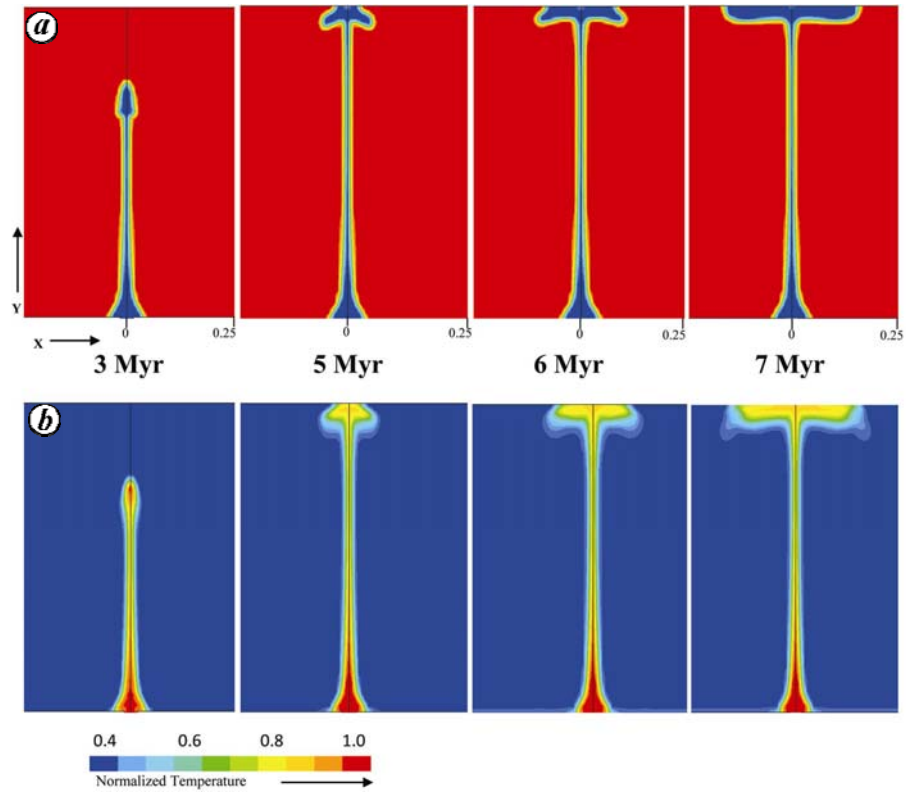

Figure 4. Successive stages of the plume head geometry in model simulations performed with a higher influx rate (Re = 18). The values of $\Delta\rho$ and R are the same as in the model shown in Figure 3. Plume shapes defined by (***a***) phase and (***b***) thermal boundaries. Scale bar shows the normalized temperatures.

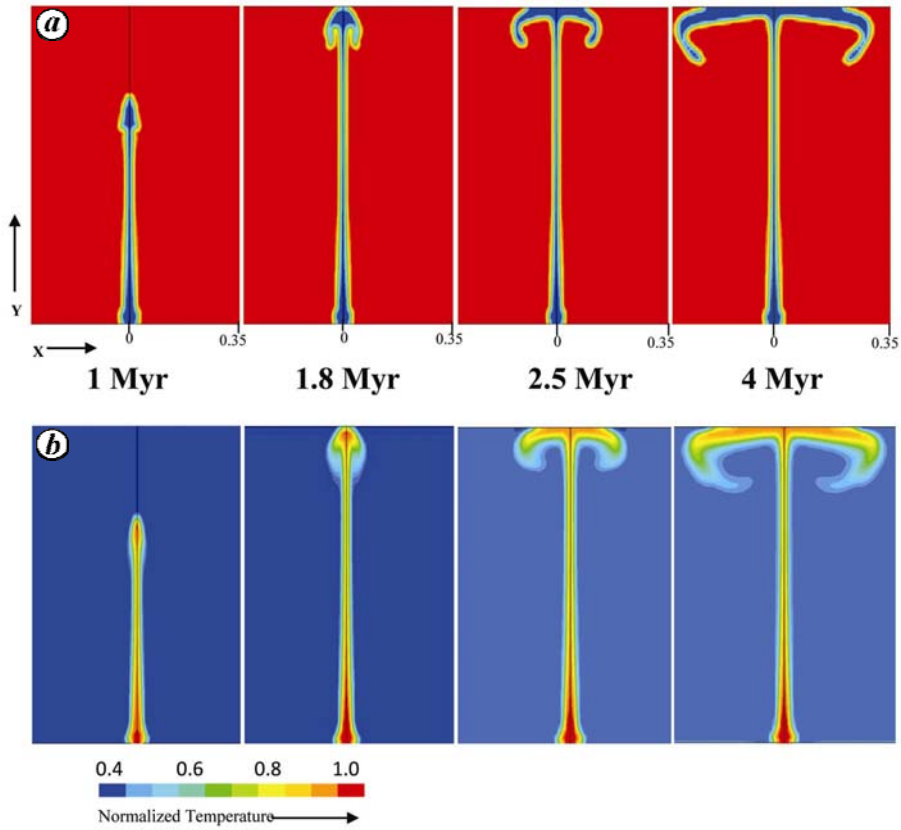

Figure 5. Development of plumes by curling mode in models with a low density contrast ($\Delta\rho = 1.1$) and a high influx rate ($Re \sim 20$). (***a***) Phase and (***b***) thermal structures.

head expanded laterally, and subsequently formed flanking geometry, which however did not show any tendency of curling in developing mushroom geometry. The plume continued to grow laterally, maintaining a constant thickness, forming a flat-shaped head at the surface. This model also showed the thermal structure grossly conforming to those defined by the phase boundary (Figure 4 *b*). However, the thermal boundaries are more diffuse compared to those in the previous models. The temperature in the plume head decreased to a larger extent, where the maximum temperature dropped to $0.7T_p$ (T_p is the initial temperature of material influx). Similarly, the tail temperature dropped to a value ($0.6T_p$) much lower than the maximum temperature in the head. The tail progressively narrowed down in diameter thermally as well as physically.

The plume mode underwent a transition with decreasing density contrast ($\Delta\rho$) under a high influx rate ($Re \sim 20$). The head curled to produce a mushroom-shaped plume structure when $\Delta\rho$ was decreased to 1.1 (Figure 5 *a*). At the initial stage the head did not grow much in size, and vertical growth of the tail was the dominating process, giving rise to a small, balloon-shaped head connected to a long tail. The head did not develop any tendency of curling until it ascended to a depth level of $0.9H$, where H is the mantle thickness. The process of curling became pronounced as the head ascended beyond this depth level, and reached the model surface (Figure 5 *a*). At this stage the plume head underwent simultaneously curling and lateral spreading in the horizontal direction, resulting in typical mushroom-shaped geometry, as reported widely in the literature[7,17,20,21]. During the growth of the plume head the tail attained a steady diameter of 50 km, which remained unchanged throughout the plume history. This model developed the thermal structure discernibly different from that obtained from the phase boundary, especially at the early stages of plume evolution (Figure 5 *b*). For example, the phase boundary of the plume head at $t = 1.8$ Myr shows curling, whereas the corresponding thermal boundary describes grossly balloon-shaped geometry. In the advanced stage (e.g. $t = 4$ Myr) the thermal structure curls, but quite weakly compared to the phase boundary. Furthermore, the thermal boundary is strongly diffused, and the high-temperature regimes localize at the shallow level, showing little effects of curling.

We investigated the thermal structures of plumes from temperature profile across the plume head. The ballooning and curling types show contrasting temperature profiles (Figure 6 *a*). Ballooning-type of plumes are characterized by steeper thermal gradients across their boundaries, compared to that in the curling-type. Secondly, the temperature remains laterally more uniform in

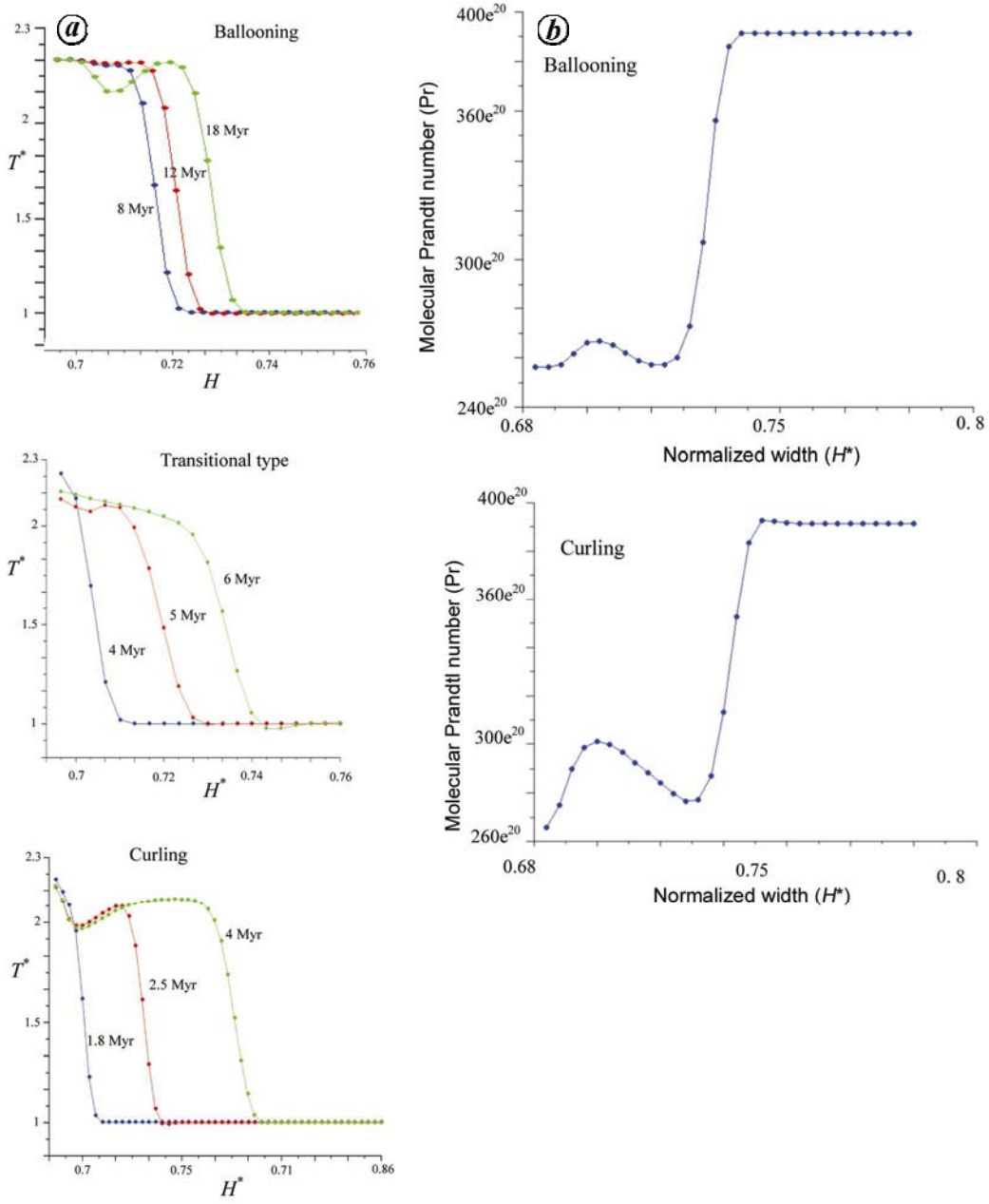

Figure 6. ***a***, Temperature profile of plume head along a horizontal, central line passing through the head. Both temperature and horizontal distance have been shown by their values normalized with respect to the corresponding far-field temperatures and the horizontal model dimension respectively. ***b***, Variation of Prandtl number across the plume head.

case of ballooning. In the advanced stage the profile shows a temperature drop inside the head, which resulted possibly from a secondary convection process operating inside the plume head (Figure 7; details are discussed later). On the other hand, the curling type shows a strongly heterogeneous temperature distribution within its head, characterized by pronounced temperature drop at a distance of 125 km from the plume axis. The locations of minimum temperatures as well as the corresponding values remain unchanged during the lateral progression of the thermal boundary. For the transitional variety of the plume, the temperature profiles show decreasing temperature from the centre to periphery of the head without any temperature well. In a very advanced stage there is a weak temperature minimum at the outermost thermal boundary. The plume temperature along the axis also varies with the mode of plume ascent. For the ballooning type $T^* = 2.3$, which slightly decreases to 2.1 for the curling type. Both the modes do not involve any pronounced variations in the axial temperature in the course of plume

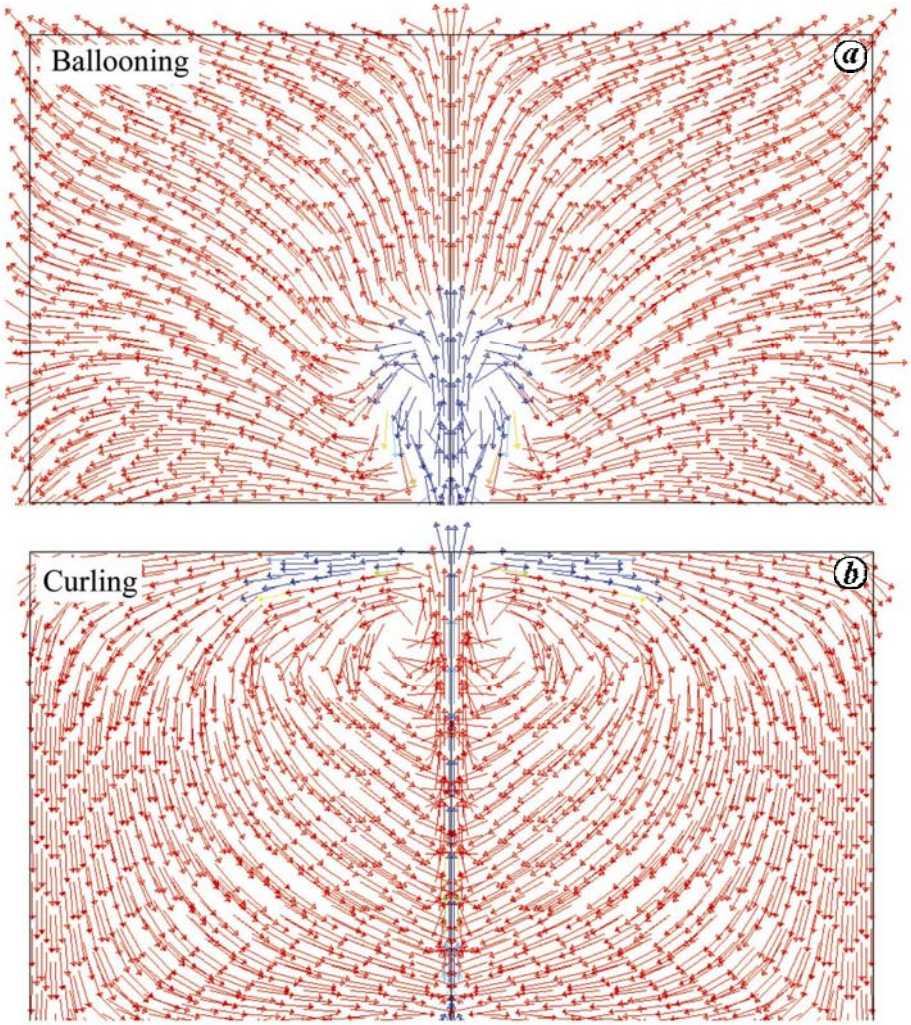

Figure 7. Contrasting patterns of advection driven by plume ascent in (***a***) ballooning and (***b***) curling modes.

growth. The transitional variety shows slight fluctuations in the axial temperature. We also estimated the *Pr* on a horizontal line passing centrally across the plume head (Figure 6 *b*). The maximum *Pr* inside the head is in the order of 10^{22}. The *Pr* value increases steeply across the plume head boundary, indicating weaker thermal diffusion rates outside the plume. In general, the curling type is associated with relative higher *Pr* compared to the ballooning type. The former is thus found to be much more effective for viscous diffusion.

Plume-controlled thermo-mechanical flow patterns

Ascending plumes induce viscous flows in the ambient mantle by a combined effect of thermal and mechanical forces. The flow patterns depend on the mode of plume ascent. For the ballooning mode, it is characterized by entirely divergent motion (Figure 7 *a*), implying that ballooning plumes cannot involve any material entrainment during their ascent. However, inside the plumes convection type of flow occurs due to thermal effects, giving rise to symmetrical vortices. This internal convection tends to die out when the ballooning type is replaced by curling type. In contrary, the curling plume develops a large-scale vortex-type of motion in the ambient mantle (Figure 7 *b*). This type of motion explains the curling behaviour of the plume head as well as strong effects of entrainment of ambient mantle materials. The vortex motion circulates the colder materials in contact with the tail walls, leading to a discernible temperature drop in plume material flowing through the tail.

Natural plume shapes

Previous (e.g. Lin and van Keken[7]) as well as the present simulation experiments show the curling mode of ascent, giving rise to mushroom-shaped plumes. Similar plume shapes have also been demonstrated from physical experiments[24]. To the best of our knowledge, typical mushroom-shaped plumes are yet to be reported from

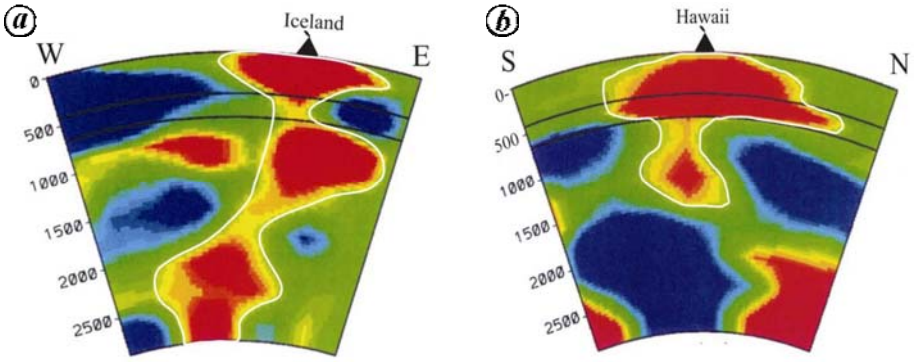

Figure 8. Seismic tomographic images of balloon-shaped plumes beneath (***a***) Iceland hotspot and (***b***) Hawaii Islands (after Zhao[3]).

geophysical evidences. Using the seismic tomography methods many workers have detected the mantle plumes rooted to the core–mantle boundary (e.g. Zhao[3]). On the other hand, some workers have employed a thermodynamic approach to synthesize the possible seismic structures (based on *P*- and *S*-wave velocity) from a set of dynamical plume models with different morphologies[48]. However, the plumes occur mostly as a train of discrete balloon-shaped heads, as observed beneath Iceland hotspot (Figure 8 *a*) and Hawaii islands (Figure 8 *b*)[49,50]. They never show typical mushroom-shaped geometry, as observed in numerical and analogue experiments.

A basic question that follows from this discussion is why the curling mode is uncommon in nature. To address this issue, we need to understand the nature of boundary detected by seismic tomography, more specifically physical or any other attributes related to the plume-induced thermal conditions. Our study suggests that the plume shapes defined by the phase boundary (i.e. physical boundary between the plume and ambient mantle materials) can develop strongly curling heads (Figure 5 *a*). The curling geometry becomes less pronounced when the same plume is defined by a thermal boundary (Figure 5 *b*). In case, the thermal structure shows balloon-shaped geometry even the plume describes spectacular curling of the phase boundary. It thus appears that seismic anomalies are sensitive to temperature-dependent material properties such as shear modulus, and reveal the thermal boundaries, rather than the corresponding phase boundaries.

Conclusions

The study leads us to conclude the following points. (1) The two extreme shapes of mantle plume heads detected by the phase boundary – ballooning and curling, depend mainly on the mantle–plume density contrast and the rate of material influx into plume tails. The ballooning occurs in conditions of high density contrasts and low influx rates, which undergoes transformation into the curling shapes as the condition is reversed (i.e. low density contrasts and high influx rates). (2) The thermal structure of plumes considerably differs from that defined by the phase boundary in case of the curling mode. Consequently, the thermal plume geometry, irrespective of its mode shows dominantly balloon-type shape, as reported from seismic tomography. (3) In case of ballooning mode, the thermal plume boundary is sharp, which turns to be diffused as the mode is replaced by curling. The thermal state inside the head becomes heterogeneous, showing temperature drop to a minimum. (4) The Prandtl number (ratio of viscous/thermal diffusion rates) estimated for the plume head is in the order of 10^{22}, showing slightly higher values for the curling mode. (5) The flows in the ambient mantle driven by the plume ascent in the ballooning mode are characterized by strong divergence, showing no close streamlines. In contrast, the curling type develops large-scale vortex motions with their locations moving upward with the plume ascent.

1. Morgan, W., Convection plumes in the lower mantle. *Nature*, 1971, **230**, 42–43; doi:10.1038/230042a0.
2. White, R. and McKenzie, D., Magmatism at rift zones: the generation of volcanic continental margins and flood basalts. *J. Geophys. Res.*, 1989, **94**, 7685–7729.
3. Zhao, D., Seismic structure and origin of hotspots and mantle plumes. *Earth Planet. Sci. Lett*., 2001, **192**, 251–265.
4. Turcotte, D. L. and Schubert, G., Geodynamics, Cambridge University Press, 1982, 1st edn, pp. 254–274.
5. Griffiths, R. W. and Campbell, I. H., Stirring and structure in mantle starting plumes. *Earth Planet. Sci. Lett.*, 1990, **99**, 66–78.
6. Davaille, A. and Vatteville, J., On the transient nature of mantle plumes. *Geophys. Res. Lett.*, 2005, **32**, doi:10.1029/2005GL-023029.
7. Lin, S. C. and van Keken, P. E., Dynamics of thermochemical plumes: 2. Complexity of plume structures and its implications for mapping mantle plumes. *Geochem. Geophys. Geosyst*., 2006, **7**, Q03003; doi: 10.1029/2005GC001072.
8. Jellinek, A. M. and Manga, M., The influence of a chemical boundary layer on the fixity, spacing and lifetime of mantle plumes. *Nature*, 2002, **418**, 760–763; doi:10.1038/nature00979.
9. Nakakuki, T., Sato, H. and Fujimoto, H., Interaction of the upwelling plume with the phase and chemical boundary at the 670 km discontinuity: effects of temperature-dependent viscosity. *Earth Planet. Sci. Lett.*, 2004, **121**, 369–384.

10. Campbell, I. H., Testing the plume theory. *Chem. Geol*., 2007, **241**, 153–176.
11. Kellogg, L. H., Interaction of plumes with a compositional boundary at 670 km. *Geophys Res Lett.*, 1991, **18**, 865; doi:10.1029/91GL01066.
12. Manga, M., Stone, H. A. and O'Connell, R. J., The interaction of plume heads with compositional discontinuities in the Earth's mantle. *J. Geophys. Res*., 1993, **98**, 19979–19990.
13. Wullner, U. and Davies, G. F., Numerical evaluation of mantle plume spacing, size, flow rates and unsteadiness. *J. Geophys. Res.*, 1999, **104**, 7377–7387.
14. Farnetani, C. G. and Samuel, H., Beyond the thermal plume paradigm. *Geophys. Res. Lett.*, 2005, L07311; doi:10.1029/2005GL022360.
15. Kumagai, I. and Kurita, K., On the fate of thermally buoyant mantle plumes at density interfaces. *Earth Planet. Sci. Lett.*, 2007, **254**, 180–193.
16. Tosi, N. and Yuen, D. A., Bent-shaped plumes and horizontal channel flow beneath the 660 km discontinuity. *Earth Planet. Sci. Lett.*, 2011, **312**, 348–359.
17. Farnetani, C. G., Legras, B. and Tackley, P. J., Mixing and deformation in mantle plumes. *Earth Planet. Sci. Lett.*, 2002, **196**, 1–15.
18. Kaminski, E. and Jaupart, C., Laminar starting plumes in high-Prandtl-number fluids. *J. Fluid Mech.*, 2003, **478**, 287–298; doi:10.1017/S0022112002003233.
19. Schubert, G., Tsepelev, I. and Korotkii, A., Three-dimensional forward and backward numerical modeling of mantle plume evolution: effects of thermal diffusion. *J. Geophys. Res*., 2006, **111**, B06401; doi:10.1029/2005JB003782.
20. Tan, Ka-K., Thorpe, R. B. and Zhao, Z., On predicting mantle mushroom plumes. *Geosci. Front.*, 2011, **2**, 223–235.
21. Shlien, D. J., Some laminar thermal and plume experiments. *Phys. Fluids*, 1976, **19**, doi:10.1063/1.861614.
22. Whitehead, J. A., Buoyancy driven instabilities of low viscosity zones as models of magma-rich zones. *J. Geophys. Res*. *B*, 1986, **91**, 9303–9314.
23. Olson, P. and Singer, H., Creeping plumes. *J. Fluid Mech.*, 1985, **158**, 511–531.
24. Whitehead, J. A. and Luther, D. S., Dynamics of laboratory diapir and plume models. *J. Geophys. Res.*, 1975, **80**, 705–717.
25. Kellogg, L. H. and King, S. D., The effect of temperature dependent viscosity on the structure of new plumes in the mantle: results of a finite element model in a spherical, axisymmetric shell. *Earth Planet. Sci. Lett.*, 1997, **148**, 13–26.
26. Kumagai, I., On the anatomy of mantle plumes: effect of the viscosity ratio on entrainment and stirring. *Earth Planet. Sci. Lett.*, 2002, **198**, 211–224.
27. Ribe, N. M., Davaille, A. and Christensen, U. R., Fluid dynamics of mantle plumes. In *Mantle Plumes – A Multi-Disciplinary Approach* (eds Ritter, J. R. R. and Christensen, U. R.), Springer, New York, 2007, pp. 1–48.
28. Kumagai, I., Davaille, A., Kurita, K. and Stutzmann, E., Mantle plumes: thin, fat, successful, or failing? Constraints to explain hot spot volcanism through time and space. *Geophys. Res. Lett.*, 2008, **35**, L16301; doi:10.1029/2008GL035079.
29. Yuen, D. A. and Peltier, W. R., Mantle plumes and the thermal stability of the *D″* layer. *Geophys. Res. Lett*., 1980, **7**, 625–628.
30. Stacey, F. D. and Loper, D. E., The thermal boundary layer interpretation of *D″* and its role as a plume source. *Phys. Earth Planet. Inter*., 1983, **33**, 45–55.
31. Griffiths, R. W., Thermals in extremely viscous fluids, including the effects of temperature-dependent viscosity. *J. Fluid Mech.*, 1985, **166**, 115–138.
32. Coulliette, D. L. and Loper, D. E., Experimental, numerical and analytical models of mantle starting plumes. *Phys. Earth Planet. Inter.*, 1995, **92**, 143–167.
33. Tan, E. and Gurnis, M., Metastable superplumes and mantle compressibility. *Geophys. Res. Lett*., 2005, **32**, L20307; doi:10.1029/2005GL024190.
34. Lee, C. and King, S. D., Effect of mantle compressibility on the thermal and flow structures of the subduction zones. *Geochem. Geophys. Geosyst*., 2009, **10**, Q01006; doi:10.1029/2008GC002151.
35. Leng, W. and Gurnis, M., Shape of thermal plumes in a compressible mantle with depth-dependent viscosity. *Geophys. Res. Lett.*, 2012, **39**, L05310; doi:10.1029/2012GL050959.
36. Hager, B. H. and Richards, M. A., Long-wavelength variations in Earth's geoid: physical models and dynamical implications. *Philos. Trans. R. Soc. London, Ser. A*, 1989, **328**, 309–327; doi:10.1098/rsta.0038.
37. Tirone, M., Ganguly, J. and Morgan, J. P., Modeling petrological geodynamics in the Earth's mantle. *Geochem. Geophys. Geosyst.*, 2009, **10**, Q04012; doi:10.1029/2008GC002168.
38. Paulson, A. and Richards, M. A., On the resolution of radial viscosity structure in modeling long-wavelength postglacial rebound data. *Geophys. J. Int.*, 2009, **179**, 1516–1526.
39. Terasaka, K. and Tsuge, H., Bubble formation at a single orifice in highly viscous liquids. *J. Chem. Eng. Jpn.*, 1990, **23**, 160–165.
40. Hirt, C. W. and Nicols, B. D., Volume of fluid (VOF) method for the dynamics of free boundaries. *J. Comput. Phys.*, 1981, **39**, 201–225.
41. Fluent 6.0 Users Guide Documentation, Fluent Inc, 2001.
42. Gopala, V. R. and Van Wachem, B. G. M., Volume of fluid methods for immiscible-fluid and free-surface flows. *Chem. Eng. J*., 2008, **141**, 204–221.
43. Jeon, S. S., Kim, S. J. and Park, G. C., CFD simulation of condensing vapor bubble using VOF model. Proceedings of World Academy of Science, Engineering and Technology, 2009, **60**, 209–215.
44. Bercovici, D., The generation of plate tectonics from mantle convection. *Earth Planet. Sci. Lett.*, 2003, **205**, 107–121.
45. Gerya, T. V. and Yuen, D. A., Rayleigh–Taylor instabilities from hydration and melting propel 'cold plumes' at subduction zones. *Earth Planet. Sci. Lett.*, 2003, **212**, 47–62.
46. Solotamov, V. S. and Barr, A. C., Onset of convection in fluids with strongly temperature-dependent, power-law viscosity. 2. Dependence on the initial perturbation. *Phys. Earth Planet. Iner*., 2007, **165**, 1–13.
47. Davaille, A., Limare, A., Touitou, F., Kumagai, I. and Vatteville, J., Anatomy of a laminar starting thermal plume at high Prandtl number. *Exp. Fluids*, 2011, **50**, 285–300.
48. Styles, E., Goes, S., van Keken, P. E., Ritsema, J. and Smith, H., Synthetic images of dynamically predicted plumes and comparison with a global tomographic mode. *Earth Planet. Sci. Lett.*, 2011, **311**, 351–363.
49. Nataf, H. C., Seismic imaging of mantle plumes. *Annu. Rev. Earth Planet. Sci*., 2000, **28**, 391–417.
50. Montelli, R., Nolet, G., Dahlen, F. A. and Masters, G., A catalogue of deep mantle plumes: New results from finite frequency tomography. *Geochem. Geophys. Geosyst.*, 2006, **7**, Q11007; doi:10.1029/2006GC001248.

ACKNOWLEDGEMENTS. We thank the SERB, DST, New Delhi for financial support through a research project. U.D. thanks the CSIR, New Delhi for providing a research fellowship.